

Calculating temperature-dependent properties of Nd₂Fe₁₄B permanent magnets by atomistic spin model simulations

Qihua Gong,¹ Min Yi,^{1,2,3,*} Richard F. L. Evans,⁴ Bai-Xiang Xu,¹ and Oliver Gutfleisch¹

¹*Institute of Materials Science, Technische Universität Darmstadt, 64287 Darmstadt, Germany*

²*State Key Lab of Mechanics and Control of Mechanical Structures & Key Lab for Intelligent Nano Materials and Devices of Ministry of Education & College of Aerospace Engineering, Nanjing University of Aeronautics and Astronautics (NUAA), Nanjing 210016, China*

³*State Key Lab for Strength and Vibration of Mechanical Structure, Xi'an Jiaotong University, Xi'an 710049, China*

⁴*Department of Physics, The University of York, York, YO10 5DD, United Kingdom*

(Dated: February 27, 2022)

Temperature-dependent magnetic properties of Nd₂Fe₁₄B permanent magnets, i.e., saturation magnetization $M_s(T)$, effective magnetic anisotropy constants $K_i^{\text{eff}}(T)$ ($i = 1, 2, 3$), domain wall width $\delta_w(T)$, and exchange stiffness constant $A_e(T)$, are calculated by using *ab-initio* informed atomistic spin model simulations. We construct the atomistic spin model Hamiltonian for Nd₂Fe₁₄B by using the Heisenberg exchange of Fe–Fe and Fe–Nd atomic pairs, the uniaxial single-ion anisotropy of Fe atoms, and the crystal-field energy of Nd ions which is approximately expanded into an energy formula featured by second, fourth, and sixth-order phenomenological anisotropy constants. After applying a temperature rescaling strategy, we show that the calculated Curie temperature, spin-reorientation phenomenon, $M_s(T)$, $\delta_w(T)$, and $K_i^{\text{eff}}(T)$ agree well with the experimental results. $A_e(T)$ is estimated through a general continuum description of the domain wall profile by mapping atomistic magnetic moments to the macroscopic magnetization. A_e is found to decrease more slowly than K_1^{eff} with increasing temperature, and approximately scale with normalized magnetization as $A_e(T) \sim m^{1.2}$. Especially, the possible domain wall configurations at temperatures below the spin-reorientation temperature and the associated δ_w and A_e are identified. This work provokes a scale bridge between *ab-initio* calculations and temperature-dependent micromagnetic simulations of Nd-Fe-B permanent magnets.

I. INTRODUCTION

Nd-Fe-B permanent magnets are critical for the key components of energy-related technologies, such as wind turbines and electro-mobility. They are also important in robotics, automation, sensors, actuators, and information technology [1–3]. Since there is increasing demand in high-end technology that permanent magnets be used at finite or elevated temperatures, the temperature-dependent properties of Nd₂Fe₁₄B, the main phase of Nd-Fe-B magnets, are of great interest. For example, these magnets are exposed to elevated temperatures in many applications such as the motors inside hybrid vehicles where the operating temperature can approach 450 K.

Modelling and simulation play an important role in the design of permanent magnets for applications at elevated temperatures. Currently, first-principles calculations and micromagnetic simulations dominate the modelling of permanent magnets. The former helps to understand the magnetic properties on the electronic-level, as well as to predict intrinsic parameters (e.g. magnetic moment, crystal field parameter, etc.) at zero temperature [4–9]. However, first-principles calculations become very challenging at finite temperature. Micromagnetic model aims at simulating the domain structure on the nano/microscale level, and is very useful when studying

the influence of microstructure (e.g. grain shape/size, grain boundary, intergranular phase, etc.) on the magnetization reversal process and the macroscopic properties of permanent magnets [10–19]. The thermal activation of nucleation at finite temperatures and its effect on the decay of coercive field in Nd-Fe-B magnets are addressed by micromagnetic simulations [20, 21], but the temperature-dependent intrinsic properties have to be already known or determined beforehand. In addition, it is well known that the micromagnetic model is essentially a continuum approximation and assumes the magnetization to be a continuous function of position. This approximation holds when the considered length scales are large enough for the atomic structure to be ignored [14, 22]. However, when the region of interest is at the same scale as the exchange length, this approximation would fail. For example, in Nd-Fe-B magnets, the amorphous grain boundary is often found to be around 2 nm (close to the micromagnetic exchange length of Nd₂Fe₁₄B). The validity of micromagnetic representation of this 2-nm region with homogenized parameters remains as an issue. A scale bridge between these two methodologies for modeling Nd-Fe-B magnets is desired. Moreover, the evaluation of temperature-dependent macroscopic parameters for micromagnetic simulations is highly nontrivial. In this aspect, there are recent attempts to study temperature-dependent effective magnetic anisotropy, saturation magnetization, and reversal process in Nd₂Fe₁₄B by using atomistic spin model simulations [23–27], based on which

* yimin@nuaa.edu.cn

the concept of a multiscale model approach for the design of advanced permanent magnets is proposed [28]. In general, an atomistic spin model is capable of calculating magnetic properties at different temperatures [29–31], in which the temperature effects can be taken into account by either Langevin-like spin dynamics or Monte Carlo simulations. Its application to permanent magnets, or more especially rare-earth permanent magnets, is still at its early stage. More efforts have to be made to either understand the gap between model simulations and experimental measurements or predict parameters over a broad range of temperatures, in order to establish the atomistic spin model as a readily available methodology for designing Nd-Fe-B magnets. In this work, following the similar framework in [24, 25, 32], we not only calculate the Curie temperature and the temperature dependent magnetization, magnetocrystalline anisotropy and domain wall width, but also add some additional new knowledge into the community of Nd-Fe-B magnets in terms of atomistic spin model simulations and temperature dependent intrinsic parameters. For example, considering the different description of spin states in the classical and quantum manner, such as the different availability of spin states in the classical atomistic spin model simulations and experiments, we determine the temperature rescaling parameter for Nd₂Fe₁₄B and figure out the difference between simulation and experimental temperatures. In this way, the calculated magnetization *vs* temperature curve shows a better agreement with the experimental one than that in [24]. In addition, except for the domain wall width at temperatures higher than the spin reorientation temperature, we also carefully examine various types of domain wall configurations and their width at temperatures lower than the spin reorientation temperature. Moreover, linking the simulation results and the micromagnetic theory, we determine the exchange stiffness for a wide range of temperatures and identify the scaling law.

Specifically, here we present an *ab-initio* informed atomistic spin model for the theoretical calculation of the Curie temperature, spin-reorientation temperature, and magnetic properties of Nd₂Fe₁₄B, such as saturation magnetization $M_s(T)$, effective magnetic anisotropy constants $K_i(T)$ ($i = 1, 2, 3$), domain wall width $\delta_w(T)$, and exchange stiffness constant $A_e(T)$ at temperatures both higher and lower than the spin reorientation temperature. The calculation results are coherent with the experimental results. Our work here provides effective parameters for micromagnetic simulations and will be useful for revealing the atomic-scale magnetic behavior in Nd-Fe-B magnets.

II. ATOMISTIC SPIN MODEL FOR Nd₂Fe₁₄B

For calculating the temperature-dependent magnetic properties, we use the atomistic spin model which treats each atom as a classic spin [29–31]. For Nd₂Fe₁₄B, the

atomistic spin Hamiltonian can be written as

$$\mathcal{H} = -\frac{1}{2} \sum_{i \neq j}^{i,j \in \text{Fe}} J_{ij}^{\text{Fe-Fe}} \mathbf{s}_i \cdot \mathbf{s}_j - \frac{1}{2} \sum_{i \in \text{Fe}}^{j \in \text{Nd}} J_{ij}^{\text{Fe-Nd}} \mathbf{s}_i \cdot \mathbf{s}_j - \sum_{i \in \text{Fe}} k_i^{\text{Fe}} (\mathbf{s}_i \cdot \mathbf{e}^z)^2 + \mathcal{H}_{\text{Nd}}^{\text{cf}}. \quad (1)$$

It should be noted that in Eq. 1 the energy terms from the external magnetic field and the dipole interaction between atomic spin moments are not included, since here we only focus on the calculation of intrinsic properties. \mathbf{s}_i is a unit vector denoting the local spin moment direction. The first two terms in Eq. 1 correspond to the Heisenberg exchange energy. They only contain the exchange interactions in Fe-Fe ($J_{ij}^{\text{Fe-Fe}}$) and Fe-Nd ($J_{ij}^{\text{Fe-Nd}}$) atomic pairs, owing to the fact that B sites are usually taken to be nonmagnetic and the interaction between Nd sites can be negligible [24, 25, 28]. The third term in Eq. 1 represents the uniaxial magnetic anisotropy energy of Fe atoms, with k_i^{Fe} as the anisotropy energy of per Fe atom and \mathbf{e}^z the z -axis unit vector. The fourth term in Eq. 1 denotes the crystal-field (CF) Hamiltonian of Nd ions, which is the main source of large magnetic anisotropy in Nd₂Fe₁₄B and can be approximated as [24, 25, 33]

$$\mathcal{H}_{\text{Nd}}^{\text{cf}} = \sum_{i \in \text{Nd}} \sum_{n=2,4,6} \alpha_n \langle r^n \rangle_{4f,i} A_{n,i}^0 \hat{\Theta}_{n,i}^0, \quad (2)$$

in which α_n is the Stevens factors, $\langle r^n \rangle_{4f,i}$ the $4f$ radial expectation value of r^n at the respective Nd site i , $A_{n,i}^0$ the CF parameters, and $\hat{\Theta}_{n,i}^0$ the Stevens operator equivalents. For Nd³⁺ ions, $\alpha_2 = -6.428 \times 10^{-3}$, $\alpha_4 = -2.911 \times 10^{-4}$, and $\alpha_6 = -3.799 \times 10^{-5}$ [34]. $\langle r^n \rangle$ values of Nd³⁺ ions can be calculated as $\langle r^2 \rangle = 1.001a_0^2$, $\langle r^4 \rangle = 2.401a_0^4$, and $\langle r^6 \rangle = 12.396a_0^6$ in which a_0 is the Bohr radius [35]. The Stevens operator equivalents are expressed as [34]

$$\begin{aligned} \hat{\Theta}_2^0 &= 3J_z^2 - \mathcal{J} \\ \hat{\Theta}_4^0 &= 35J_z^4 - 30\mathcal{J}J_z^2 + 25J_z^2 - 6\mathcal{J} + 3\mathcal{J}^2 \\ \hat{\Theta}_6^0 &= 231J_z^6 - 315\mathcal{J}J_z^4 + 735J_z^4 + 105\mathcal{J}^2J_z^2 \\ &\quad - 525\mathcal{J}J_z^2 + 294J_z^2 - 5\mathcal{J}^3 + 40\mathcal{J}^2 - 60\mathcal{J}. \end{aligned} \quad (3)$$

$J_z = J(\mathbf{s} \cdot \mathbf{e}^z)$ denotes the z -component of the total angular momentum J which is 9/2 for Nd ions [34]. $\mathcal{J} = J^2$ instead of $\mathcal{J} = J(J+1)$ is used in the classical manner [24]. The reliable first-principles calculation of high-order CF parameters in Nd₂Fe₁₄B is still challenging. Here we take the A_n^0 values which are determined from the experiment results [33], i.e. $A_2^0 = 295 \text{ K}/a_0^2$, $A_4^0 = -12.3 \text{ K}/a_0^4$, and $A_6^0 = -1.84 \text{ K}/a_0^6$. We approximately set all Nd ions with the same CF parameters. In this way, combining Eq. 2, Eq. 3, and $J_{i,z} = J(\mathbf{s}_i \cdot \mathbf{e}^z)$ yields the CF energy

$$\mathcal{H}_{\text{Nd}}^{\text{cf}} = - \sum_{i \in \text{Nd}} [k_{i,1}^{\text{Nd}} (\mathbf{s}_i \cdot \mathbf{e}^z)^2 + k_{i,2}^{\text{Nd}} (\mathbf{s}_i \cdot \mathbf{e}^z)^4 + k_{i,3}^{\text{Nd}} (\mathbf{s}_i \cdot \mathbf{e}^z)^6], \quad (4)$$

in which the parameters $k_{i,1}^{\text{Nd}}$, $k_{i,2}^{\text{Nd}}$, and $k_{i,3}^{\text{Nd}}$ are listed in Table I. The constant term in $\mathcal{H}_{\text{Nd}}^{\text{cf}}$ is not important and thus not presented in Eq. 4. The magnetocrystalline anisotropy energy of the Fe sublattice and the magnetic moments of each atom, as listed in Table I, are taken from the previous first-principles calculations [24, 36]. The exchange parameters $J_{ij}^{\text{Fe-Fe}}$ and $J_{ij}^{\text{Fe-Nd}}$ in Eq. 1 are evaluated in the relaxed unit cell (lattice parameters are kept constant as $a = b = 8.76$ Å, $c = 12.13$ Å and the thermal expansion is not considered) by using OpenMX [37–40]. The calculation of Heisenberg exchange parameters J_{ij} between two different atomic sites i and j is implemented in OpenMX by using the magnetic-force theorem (follow the original formalism by Liechtenstein et al. [37]) and its extension to the nonorthogonal LCPAO (linear combination of pseudoatomic orbitals) method [38]. In detail, J_{ij} is estimated as a response to small spin tiltings (as a perturbation) from the given converged solution, as shown the detailed formulation in [37–39]. More application examples of OpenMX in calculating Heisenberg exchange parameters are reported by the OpenMX’s developers in the literature [38–41]. In fact, the unit cell here is already very large and thus the lattice translation vectors have negligible influence on the calculated J_{ij} . Indeed, our additional calculations of the $2 \times 1 \times 1$ and $2 \times 2 \times 1$ supercells show that the influence of the adopted cell size on the calculated J_{ij} can be ignored, as shown in Fig. 1. Therefore, the calculated J_{ij} here can be used in the Heisenberg spin model and the Monte Carlo simulations. An open-core pseudopotential for Nd is used, with the $4f$ electrons put in the core and not treated as valence electrons. For the many local-orbital-based methods in OpenMX, the basis set of each atom should be chosen. We use a notation of $sN_s pN_p dN_d fN_f$ to represent the basis-set choice for a given atom. For example, $s1p2d3$ denotes that one s , two p , and three d orbitals are taken as a basis set. According to the previous work [7], the basis sets for Nd, Fe, and B atoms are chosen as $s2p2d2$, $s2p2d2$, and $s2p2$, with cutoff radii of 8.0, 6.0, and 7.0 a.u., respectively. We use a $5 \times 5 \times 4$ k -point mesh, and a 500-Ry cutoff energy. The convergence criteria for the selfconsistent calculation is 10^{-6} Hartree. The calculated exchange parameters are further calibrated (interactions of Fe–Fe and Fe–Nd are rescaled by 2 and 0.9, respectively) by checking the results from the atomistic spin model simulation of $\text{Nd}_2\text{Fe}_{14}\text{B}$, and are shown in Fig. 1. It can be found that the total magnetic moment of Nd ions is ferromagnetically coupled to Fe moments, and the exchange of Fe–Fe pairs is 3–10 times stronger as that of Fe–Nd pairs. Previous studies have shown that the cutoff radius (within which exchange parameters are calculated) affect the magnetization at higher temperatures [24]. In order to reduce the computational cost, as a simplification, here we only calculate exchange parameters within the nearest-neighbor approximation. The effect from longer-range exchange interactions is not included. For $\text{Nd}_2\text{Fe}_{14}\text{B}$ system, the nearest-neighbor exchange interactions dominate while the longer-range ones are less

important. In the following we will show that the calculated macroscopic properties from this simplification are in line with the previous work [24] and the experimental report [42–44], without significant disparity. It should be noted that the micromagnetic exchange length is evaluated from the micromagnetic model in the framework of continuum picture without information from the atomistic spin at each atomic site. The micromagnetic exchange length governs the width of the transition between magnetic domains. In contrast, the exchange parameters describe the interaction between each pair of atomistic spins at specific atomic sites. They are in the framework of discrete picture in the atomistic spin scale. Thus, the micromagnetic exchange is not a direct indicator for the cutoff radius of the exchange interaction in the atomistic spin model.

After parameterization, the atomistic spin model in Eq. 1 is implemented in VAMPIRE [30]. For calculating the Curie temperature and temperature-dependent magnetization, the Monte Carlo Metropolis method is adopted, using a sample with $10 \times 10 \times 10$ unit cells and periodic boundary conditions in all three directions. After performing 10,000 Monte Carlo steps at each temperature, the equilibrium properties of the system are calculated by averaging the magnetic moments over a further 10,000 steps. It should be noted that by performing calculations at different steps, we find the results remain the same after Monte Carlo steps exceed 10,000. For the calculation of effective magnetic anisotropy constants at different temperatures, we use the constrained Monte-Carlo method [30, 45]. We constrain the direction of the global magnetization at a fixed polar angle (θ) while allow the individual spins to vary. In this way, we can calculate the restoring torque acting on the magnetization as a function of θ , from which the effective magnetic anisotropy constants can be obtained by fitting. When calculating domain wall width, we apply the spin dynamics approach and the Heun integration scheme. A sharp Bloch-like domain wall (wall plane perpendicular to x

TABLE I. Magnetic moments and atomic-site resolved magnetic anisotropy energy of each crystallographically equivalent atom.

Atom	μ_i (μ_B)	k_i ($\times 10^{-21}$ J)
		k_i^{Nd}
Nd(4g)	2.86	$k_{i,1}^{\text{Nd}} = -4.935$
Nd(4f)	2.871	$k_{i,2}^{\text{Nd}} = 25.98$
		$k_{i,3}^{\text{Nd}} = -22.94$
		k_i^{Fe}
Fe(4c)	2.531	-0.342
Fe(4e)	1.874	-0.0048
Fe(8j ₂)	2.629	0.093
Fe(8j ₁)	2.298	0.171
Fe(16k ₂)	2.206	0.0608
Fe(16k ₁)	2.063	0.0880

axis) in the middle of the sample with $N_x \times N_y \times N_z$ unit cells is set as the initial condition. The system with the demagnetizing field included further relaxes from this initial condition by 100,000 steps with a time step of 1 fs. The final domain configuration is determined by averaging the magnetic moment distribution of 100 states at 90.1, 90.2, 90.3, ..., 100 ps.

III. RESULTS AND DISCUSSION

A. Curie temperature and saturation magnetization

The calculated temperature-dependent magnetization curve for $\text{Nd}_2\text{Fe}_{14}\text{B}$ is shown in Fig. 2(a). For a classical spin model, the simulated magnetization can be related to temperature through the function [30]

$$m = M_s(T)/M_0 = (1 - T/T_c)^\beta, \quad (5)$$

in which $M_s(T)$ is the temperature dependent saturation magnetization, M_0 denotes the saturation magnetization at zero K, T_c is the Curie temperature, and β is an exponent. Direct fitting the simulation data by Eq. 5 gives $T_c = 602$ K and $\beta = 0.418$. The calculated T_c matches well with the experimental data [43].

However, it can be found from Fig. 2(a) that only the simulation results around the Curie temperature agree with the experimental measurement. This disparity could be related to the following two aspects. Firstly, the exchange parameters could vary when temperature changes, as the case for Fe shown in [46]. At high temperatures, there may exist disordered local moment (DLM)

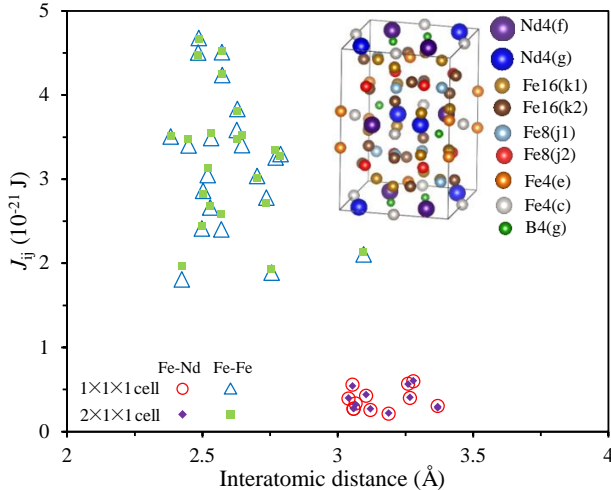


FIG. 1. Exchange parameters J_{ij} as a function of interatomic distance, with the nearest neighbor considered. Inset: unit cell of $\text{Nd}_2\text{Fe}_{14}\text{B}$ showing different kinds of crystallographically equivalent atoms. The results of $2 \times 1 \times 1$ supercell are also presented to show the independence of J_{ij} on the calculated cell size.

state [47] and thus different exchange parameters and magnetization. However, the calculation of temperature dependent exchange parameters by first-principles methods is still challenging for the complicated $\text{Nd}_2\text{Fe}_{14}\text{B}$. Nevertheless, using the constant exchange parameters, the Curie temperature of $\text{Nd}_2\text{Fe}_{14}\text{B}$ is well predicted in Fig. 2(a). Apart from the possible reason related to temperature or DLM-state dependent exchange parameters, we think the distinction between the quantum model and the classical model should also contribute to the deviation in Fig. 2(a), as thoroughly discussed in [48]. Atomistic spin model is a classical model which considers localized classical atomistic spins with unrestricted and continuous values. In contrast, the experimental measurement spontaneously includes the manifestation of a quantum system which only allows particular eigenvalues. It indicates more available states in the classical model than in experiments. The macroscopic magnetization obtained at simulation temperature T_{sim} should be achieved at higher temperature T_{exp} in experiments. For this reason, there should be a mapping between T_{sim} and T_{exp} . Here we adopt the temperature rescaling method, as proposed in the previous work [48], to determine this mapping. The (internal) simulation temperature T_{sim} is rescaled so that the equilibrium magnetization at the input experimental (external) temperature T_{exp} agrees with the experimental result, i.e.

$$T_{\text{sim}}/T_c = (T_{\text{exp}}/T_c)^\alpha, \quad (6)$$

in which α is the rescaling parameter which can be fitted. The physical interpretation of the rescaling is that at low temperatures the allowed spin fluctuations in the classical limit are overestimated, and so this corresponds to a higher effective temperature than given in the simulation (i.e. $T_{\text{exp}} > T_{\text{sim}}$) [48]. The physical origin of α may be relate to the different availability of spin states in the classical atomistic spin model simulation and the experiment. However, it would be interesting to apply detailed first-principles calculations to delineate the origin. For detailed discussion on the temperature rescaling, the readers are referred to [48]. Applying the temperature rescaling Eq. 6 to the simulation data and directly comparing the rescaled data with the experimental data, we fit the parameter α as 1.802. After these operations, we can see in Fig. 2(a) that the corrected simulation data show excellent agreement with the experimental one, and both can be described by the Curie-Bloch equation

$$m = M_s(T)/M_0 = [1 - (T/T_c)^\alpha]^\beta \quad (7)$$

with the fitted parameters $\alpha = 1.802$ and $\beta = 0.418$.

Calculating the total magnetic moments per volume, we then obtain the temperature dependent saturation magnetization $M_s(T)$ from the corrected simulation data. $M_s(T)$ agrees well with the experimental data [43], as shown in Fig. 2(b). The spin reorientation phenomenon can also be captured by atomistic spin simulations, as shown in Fig. 2(c). The simulated M_z in Fig. 2(c) firstly

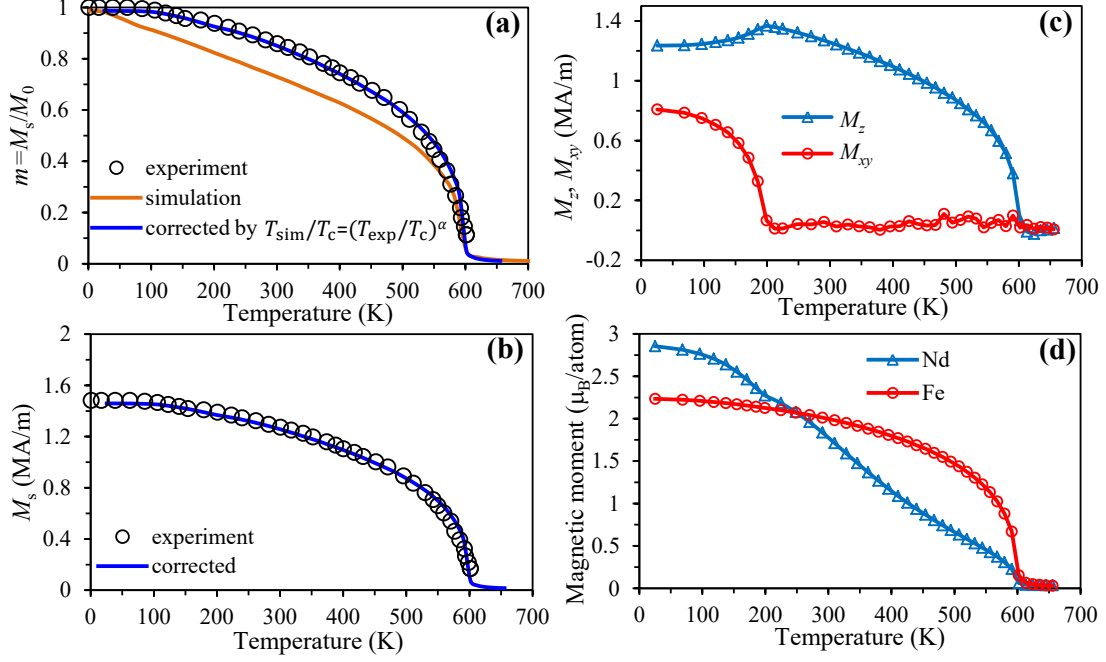


FIG. 2. Temperature dependence of (a) (b) the magnetization amplitude, (c) the magnetization components M_z and M_{xy} , and (d) the magnetic moment per atom in Nd and Fe sublattices. The corrected curves are plotted by $\alpha = 1.802$. The experimental results are taken from [43].

increases and then decreases with the increasing temperature. By comparing M_z in Fig. 2(c) to M_s in Fig. 2(b), it can be estimated that the tilting angle of the magnetization direction away from the z -axis is around 32° at $T = 25$ K. The simulated spin reorientation temperature is around 180 K, higher than the experimental value around 150 K. This deviation may be related to the low quality of the temperature rescaling at low temperature. Nevertheless, the results on spin reorientation are in line with the experimental observations [33, 43, 44]. Meanwhile, it can be seen from Fig. 2(d) that as temperature increases, the magnetization of Nd sublattice decreases faster than that of Fe sublattice. This is due to the strong exchange coupling in Fe sublattice and indicates that Fe sublattice is responsible for the magnetic order.

B. Effective magnetic anisotropy

In order to determine the effective magnetic anisotropy constants, we have to calculate the system energy when the global magnetization is aligned along different directions. This can be done through the calculation of torque. In the constrained Monte Carlo scheme, we fix the azimuthal angle at zero degree and gradually change polar angle from 0 to 90 degree, i.e., the global magnetization is rotated in the z - x plane and only the torque component T_y is nonzero. The total internal torque T_y is calculated from the thermodynamic average and transferred into the energy per volume, as shown in Fig. 3(a). It can be seen

that at low temperature (e.g. 25 and 100 K) T_y is positive when θ is close to the z /[001] axis, indicating a spontaneous deviation of the global magnetization from the z /[001] axis. This result is in line with the easy-cone type of anisotropy and the spin tilting away from z /[001] axis (Fig. 2(c)) at low temperature. At high temperature, T_y is always negative and thus there is a revert torque for driving the global magnetization towards the z /[001] axis, implying an easy-axis type of anisotropy.

After obtaining the temperature dependent T_y , the free energy (F) of the magnetic system can be related to the work done by the torque acting on the whole system, i.e.

$$F(\theta, T) = - \int_0^\theta T_y(\Theta, T) d\Theta. \quad (8)$$

Integrating the data in Fig. 3(a) through Eq. 8 gives the free-energy curves in Fig. 3(b). It can be seen that at 25 K, F shows a local minimum at $\theta \approx 32^\circ$, reflecting the spin tilting away from z /[001] axis. The effective magnetic anisotropy constants can be determined through the fitting of F curves by the phenomenological six-order formula

$$F(\theta, T) = K_1^{\text{eff}}(T) \sin^2 \theta + K_2^{\text{eff}}(T) \sin^4 \theta + K_3^{\text{eff}}(T) \sin^6 \theta, \quad (9)$$

in which K_1^{eff} , K_2^{eff} , and K_3^{eff} are the macroscopically effective second-, fourth-, and sixth-order anisotropy constants, respectively. The fitting results are presented in Fig. 3(c) and compared to the experimental measurement [42]. We can see that below 150 K, K_1^{eff} is negative and both K_2^{eff} and K_3^{eff} play a critical role, agreeing

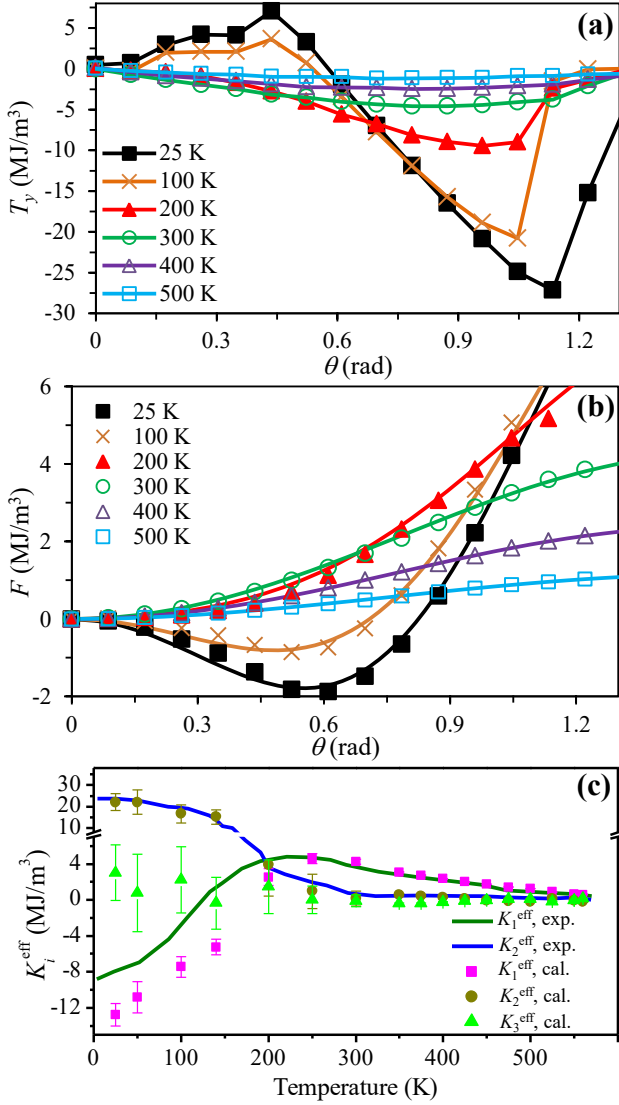


FIG. 3. (a) Internal torque density $T_y(\theta)$ and (b) free energy density $F(\theta)$ at different temperatures. (c) Temperature dependent experimental and calculated effective magnetic anisotropy constants K_i^{eff} ($i = 1, 2, 3$).

with the cone-type anisotropy of Nd₂Fe₁₄B at low temperature. After 250 K, K_1^{eff} dominates and K_2^{eff} and K_3^{eff} are relatively small. At 300 K, our calculated results are: $K_1^{\text{eff}} = 4.26$ MJ/m³, $K_2^{\text{eff}} = 0.15$ MJ/m³, and $K_3^{\text{eff}} = -0.10$ MJ/m³. At higher temperature, K_2^{eff} and K_3^{eff} almost vanish. The calculated temperature dependence of K_i^{eff} in Fig. 3(c) agrees reasonably with the previous experimental measurement [42, 43, 49] and theoretical calculations [24, 50].

C. Domain wall

Due to the different anisotropy types at low temperature (cone-type anisotropy) and high temperature (easy-

axis anisotropy) in Nd₂Fe₁₄B, the domain wall will also be distinct. At temperatures lower than the spin reorientation temperature, a number of possible variants of domain-wall types have been observed due to the cone-type anisotropy [51, 52]. For hard materials (Nd-Fe-B permanent magnets here) with dominant magnetocrystalline anisotropy, the typical domain wall profile is of the Bloch type, i.e. the magnetization is parallel to the easy axis (z or c axis for Nd₂Fe₁₄B) in the two domains separated by a domain wall perpendicular to x (a) axis. Hence, here we study the Bloch-like domain walls, with the wall plane perpendicular to x axis, as shown in Figs. 4 and 5. We consider three types of Bloch-like domain walls at low temperatures in Fig. 4. More complicated domain walls with the wall plane perpendicular to different crystallographic axes will be investigated in our next work. The three wall modes are described as the polar angle changing from θ_0 to $-\theta_0$ in Fig. 4(a), θ_0 to $\pi + \theta_0$ in Fig. 4(d), and θ_0 to $\pi - \theta_0$ in Fig. 4(g), with the angle through the wall as $2\theta_0$, π , and $\pi - 2\theta_0$, respectively. At temperatures higher than the spin reorientation temperature, the 180° Bloch-like domain wall with the polar angle changing from 0 to π is considered, as shown in Fig. 5(a).

For calculating the domain wall, we set the magnetic moment direction in the $y-z$ plane with a polar angle as θ_0 (i.e. tilting angle) and $-\theta_0$ (or $\pi \pm \theta_0$) in the upward and downward domain, respectively. We then relax the system to attain the distribution of magnetic moments around the domain wall, as shown in Fig. 4(a)(d)(g) and Fig. 5(a). It can be seen that at low temperature (e.g. below 200 K) the magnetic moments are uniformly distributed within the domain, and a clear transition of magnetic moment distribution from the domain wall to the domain is visually observable. In contrast, at higher temperatures (e.g. above 400 K), the effect of thermal fluctuations is stronger, so that there are some randomly distributed magnetic moments even in the domain and no obvious transition between the domain wall and domain can be intuitively identified.

In order to determine the domain wall width, we turn to the continuum description of domain wall or diffusive interface. For mapping the atomistic magnetic moments to the continuum magnetization, we divide the simulation sample with $N_x \times N_y \times N_z = 40 \times 5 \times 5$ unit cells into N_x parts along x axis. For the case of $2\theta_0$ domain wall in Fig. 4(a), the wall is very wide and thus a simulation sample with $N_x \times N_y \times N_z = 120 \times 5 \times 5$ unit cells is used. Each part (with an index of l_x , $1 \leq l_x \leq N_x$) represents $1 \times 5 \times 5$ unit cells, with its x coordinate set in its center. The magnetization of each part is calculated by dividing its total magnetic moments by its volume. In this way, we attain the magnetization components $M_i(x)$ and $M_{jk}(x)$ for each part l_x from the atomistic results in Figs. 4 and 5, i.e.

$$M_i(x) = \sum_{I \in l_x} \frac{\mu_{IS}^i}{V_{l_x}} \quad (10)$$

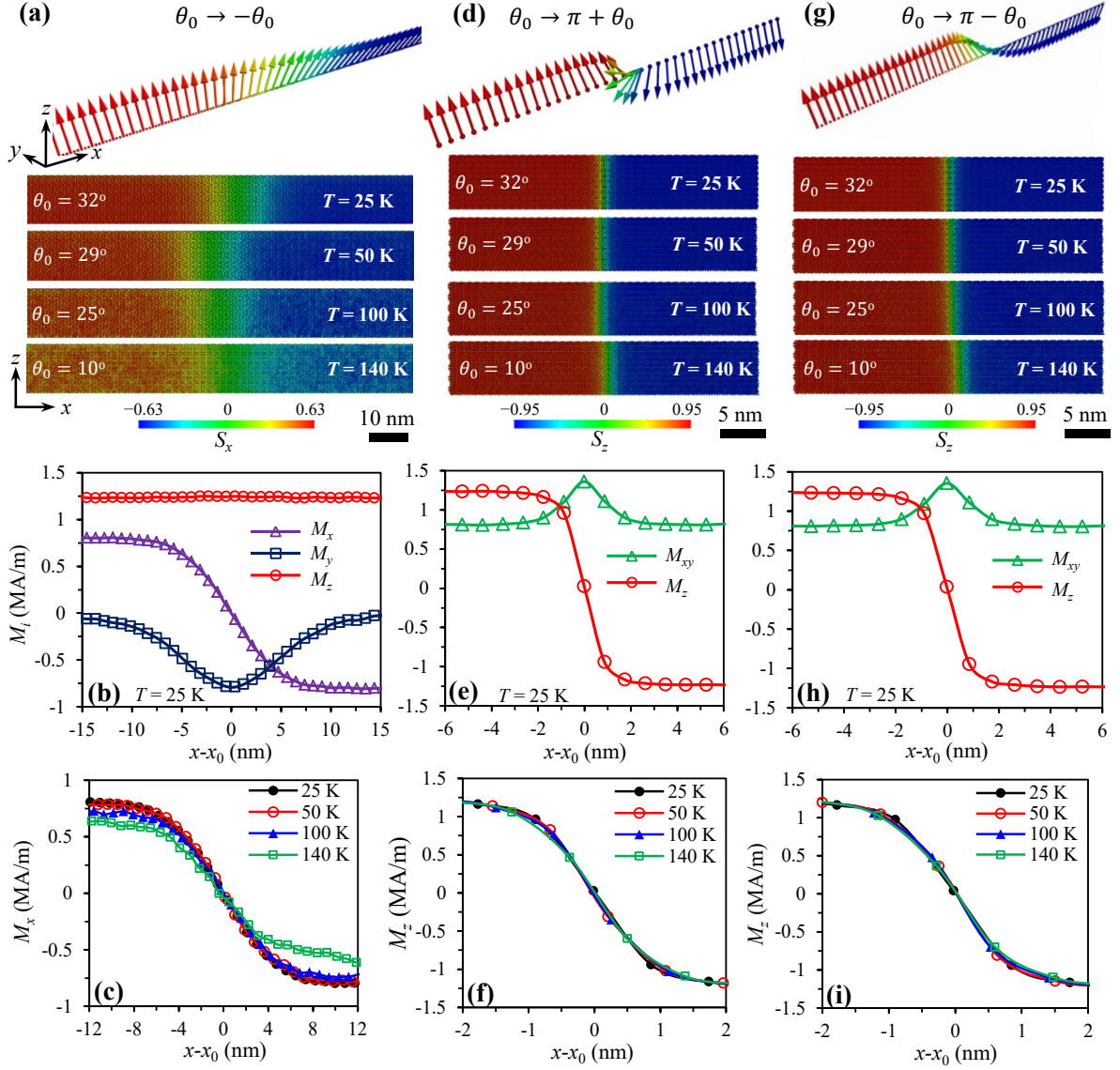


FIG. 4. (a) (d) (g) Three types of possible low-temperature (easy axis tilted from z -axis with angle θ_0) domain wall configuration displayed by the distribution of atomistic magnetic moments. The distribution of macroscopic magnetization components along x axis in the case of (b) (c) domain wall $\theta_0 \rightarrow -\theta_0$, (e) (f) domain wall $\theta_0 \rightarrow \pi + \theta_0$, and (h) (i) domain wall $\theta_0 \rightarrow \pi - \theta_0$.

and

$$M_{jk}(x) = \sum_{I \in l_x} \frac{\mu_I \sqrt{(s_I^j)^2 + (s_I^k)^2}}{V_{l_x}} \quad (11)$$

at $x = 0.5 + (l_x - 1)a$, in which μ_I is the magnetic moment of atom I in the part l_x , s_I^i ($i = x, y, z$) the spin direction components of atom I , V_{l_x} the volume of part l_x , and $a = 8.76$ Å the in-plane lattice parameter. Following the mapping in Eq. 10, we obtain the scattered data to describe the domain wall configuration, as shown in Figs. 4 and 5. In the continuum model, the domain wall or diffusive interface can be described by the hyperbolic

functions [53–55] through

$$M_i(x) = -M_s(T) \tanh \frac{x - x_0}{\delta} \quad (12)$$

or

$$M_{jk}(x) = M_s(T) / \cosh \frac{x - x_0}{\delta}, \quad (13)$$

in which x_0 is for shifting the domain wall to the center and δ is the parameter related to domain wall width δ_w by $\delta_w = \pi\delta$.

In Fig. 4, we present the domain wall profile at temperature lower than the spin reorientation temperature. For the $2\theta_0$ domain wall in Fig. 4(a), the domain wall width is quiet large. It can be found from Fig. 4(b) and

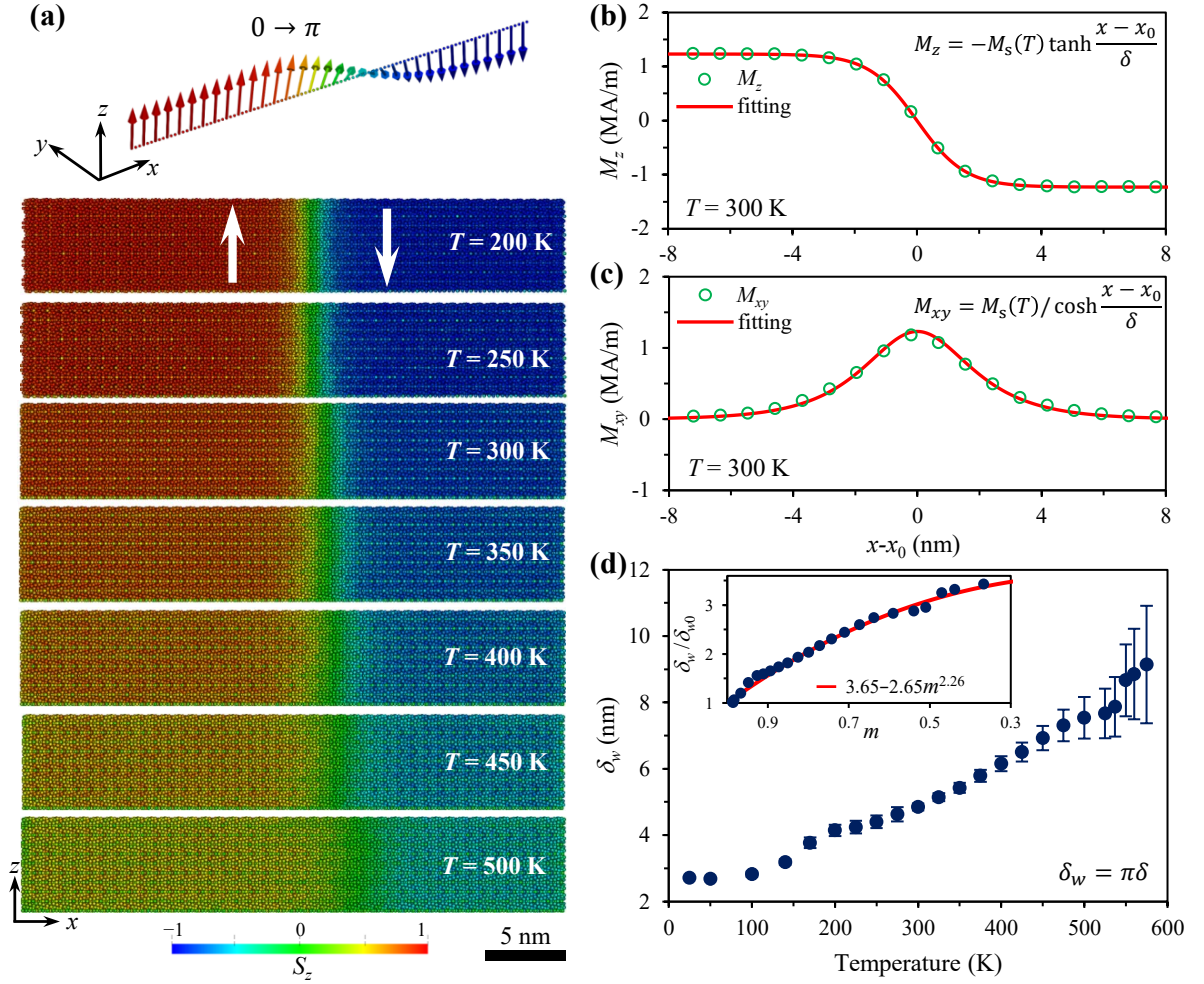


FIG. 5. (a) High-temperature (easy axis along z -axis) domain wall configuration displayed by the distribution of atomistic magnetic moments. Macroscopic (b) M_z and (c) M_{xy} distribution along x axis at $T = 300$ K. (d) Domain wall width δ_w at different temperatures. Inset in (d): δ_w scaling with magnetization as a function of $m^{2.92}$. δ_{w0} is the wall width at zero temperature.

(c) that M_z does not change along x axis, whereas M_x can be described by Eq. 12. So this wall does not satisfy the condition of constant normal component of the magnetization along the wall axis, i.e. not a Bloch-like wall. Moreover, the uniform M_z indicates constant magnetic anisotropy energy according to Eq. 9 and thus the domain wall cannot exist; because the formation of domain wall is a result of the competition between variable exchange energy and magnetic anisotropy energy. One possible explanation for the wide domain wall in Fig. 4(a) is that, the azimuthal angle also takes effects in the magnetic anisotropy energy and could contribute to the domain wall formation. The role of azimuthal angle in determining the easy direction of $\text{Nd}_2\text{Fe}_{14}\text{B}$ at low temperatures has also been addressed before [52]. However, in Eq. 9 we neglect the azimuth-angle dependence, which has to be taken into account in the following work. Here we focus on the Bloch-like wall and will not put emphasis on the wide domain wall in Fig. 4(a) as well as its width.

In contrast, the π and $\pi - 2\theta_0$ domain walls are Bloch-like and narrow, and M_z can be well described by Eq. 12, as shown in Fig. 4(e), (f), (h) and (i). The domain wall becomes slightly wider as the temperature increases from 25 K to 140 K. In addition, the wall profiles in π and $\pi - 2\theta_0$ domain walls are almost the same at a specific temperature. In the following, we will take the wall profile in $\pi - 2\theta_0$ domain wall to calculate the domain wall width and exchange stiffness at low temperatures.

At temperatures higher than the spin reorientation temperature, 180 degree Bloch-like domain walls clearly form, as shown in Fig. 5(a). Fitting the scattered data associated with the domain wall configuration by Eq. 12 or 13 can give δ and thus the domain wall width. Typical fitting results at 300 K are presented in Fig. 5(b) and (c), with $\delta = 1.55$ nm and $\delta_w = 4.87$ nm. It should be noted that at 300 K, the exchange stiffness A_e is often taken as 6.6–12 pJ/m [42, 55, 56] and K_1^{eff} as 4.2–4.5 MJ/m³ [42, 55] in the literature, corresponding to an estimated

$\delta_w = \pi\sqrt{A_e/K_1^{\text{eff}}}$ as 3.63–5.31 nm. Our calculated δ_w at 300 K falls well in the range of δ_w estimated from the literature. The measured δ_w by electron microscopy is more widely distributed, ranging from 1 to 10 nm [57–59]. The calculated domain wall width at different temperatures are summarized in Fig. 5(d). It can be found that domain wall becomes wider as the temperature increases, from $\delta_w = 2.72$ nm at 25 K to $\delta_w = 8.67$ nm at 550 K. The large standard deviation of δ_w at higher temperature is attributed to the stronger thermal fluctuations. These results are also consistent with the previous simulation results [25]. In addition, the dimensionless wall width δ_w/δ_{w0} (δ_{w0} : wall width at 0 K) can be fitted as a function of the power of dimensionless magnetization, i.e. δ_w/δ_{w0} linearly varies with $m^{2.26}$, as shown in the inset of Fig. 5(d). This is different from the low-temperature power-law scaling behavior of $m^{-0.59}$ as found in cobalt [60], possibly due to the complicated and intrinsically different crystal structure of Nd₂Fe₁₄B.

D. Exchange stiffness

The determination of temperature-dependent exchange stiffness constant $A_e(T)$ is nontrivial. At 300 K, spin-wave dispersion measurements in Nd-Fe-B magnets reveal A_e as 6.6 pJ/m [56]. In the case of uniaxial anisotropy with positive K_1^{eff} and zero K_2^{eff} and K_3^{eff} , the domain wall width can be calculated as $\delta_w = \pi\sqrt{A_e/K_1^{\text{eff}}}$, from which A_e is estimated around 7–12 pJ/m at 300 K [42, 55]. However, when K_1^{eff} is negative or K_2^{eff} and K_3^{eff} cannot be neglected, e.g. at low temperatures, the expression $\delta_w = \pi\sqrt{A_e/K_1^{\text{eff}}}$ does not work. It should be mentioned that if all K_i^{eff} are taken into account, there is no analytic solution for the Bloch wall profile [54]. In the general case, the Bloch wall profile is governed by [54]

$$dx = d\theta \sqrt{A_e(T) / [F(\theta, T) - F(\theta_0, T)]} \quad (14)$$

and thus

$$x(\theta, T) = \sqrt{A_e(T)} \int_{\theta_0}^{\theta} \frac{d\Theta}{\sqrt{F(\Theta, T) - F(\theta_0, T)}}, \quad (15)$$

in which $F(\theta, T)$ is taken from Eq. 9.

Since x is a monotonic function of θ in Eq. 15, there exists an inverse function $\theta(x, T)$. Therefore, after numerical integration of Eq. 15 with various $A_e(T)$, we attain a series of theoretical curves with x as a function of $M_z = M_s(T) \cos(\theta(x, T))$. Then we optimize $A_e(T)$ through the least-square method by comparing the simulation data to the theoretical curves. In Fig. 6(a), we plot both the simulation data points and the theoretical curves (solid lines) with the optimum $A_e(T)$. It can be found that the theoretical curves by Eq. 15 match well with the fitting results by Eq. 12. But there is intrinsic difference, i.e. Eq. 12 only gives domain wall width

which can be used to estimate A_e indirectly through $\delta_w = \pi\sqrt{A_e/K_1^{\text{eff}}}$ when K_1^{eff} is positive, whereas Eq. 15 directly gives A_e without the constraint on K_i^{eff} . The optimum $A_e(T)$ as a function of temperature is presented in Fig. 6(b). We can see that $A_e = (\delta_w/\pi)^2 K_1^{\text{eff}}$ yields reasonable results only above 300 K. In general, $A_e(T)$ shows a decreasing trend as the temperature increases. Below the spin reorientation temperature, $A_e(T)$ slowly decreases from 11.3 pJ/m at 25 K to 10.2 pJ/m at 140 K. After 200 K, $A_e(T)$ decreases much faster, from 11 pJ/m at 200 K to 3.5 pJ/m at 575 K. $A_e = 10.2$ pJ/m at 300 K is also consistent with the literature. However, A_e decreases more slowly than K_1^{eff} with increasing temper-

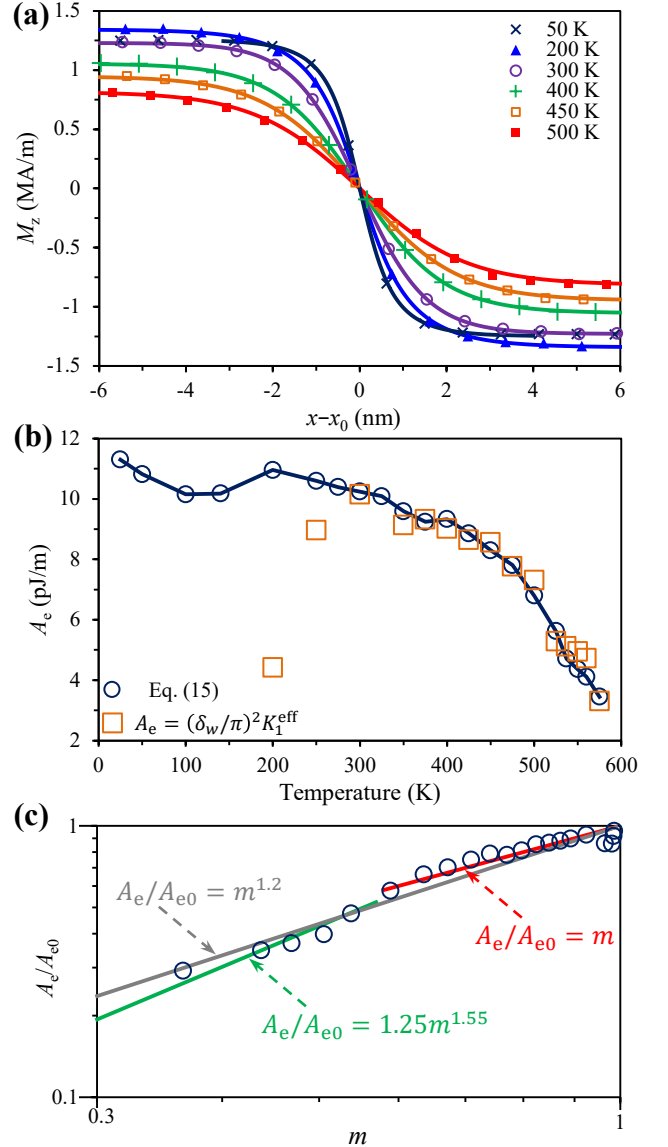


FIG. 6. (a) M_z distribution along x axis at different temperatures. (b) Calculated temperature-dependent exchange stiffness. (c) Scaling behavior of the exchange stiffness with the solid lines showing the scaling law with normalized magnetization. A_{e0} is the exchange stiffness at zero temperature.

ature. For instance, from 300 to 500 K, A_e is reduced by 34% while K_1^{eff} by 85%. This explains the wider domain wall at higher temperature in Fig. 5(d).

The scaling behavior of $A_e(T)$ is presented in Fig. 6(c). It is found that at temperatures lower than 500 K, a scaling behavior $A_e(T) \sim m$ exists. The power exponent of 1 for $\text{Nd}_2\text{Fe}_{14}\text{B}$ is much lower than 2 in the mean-field approximation (MFA), 1.66 for a simple cubic lattice, and 1.76 for FePt [61]. At temperatures close to T_c , the high-temperature behavior deviates far away from this power scaling law. In addition, fitting the data after 500 K reveals that $A_e(T)$ approximately follows the scaling law of $m^{1.55}$. Fitting all the data together with low quality gives a scaling law of $m^{1.2}$. The underlying physical reason of this distinct scaling behavior in $\text{Nd}_2\text{Fe}_{14}\text{B}$ has to be uncovered theoretically in the near future. It should be mentioned that the classical spectral density method has been attempted towards a deep theoretical understanding of the scaling behavior of exchange stiffness for simple cubic, body-centered cubic, and face-centered cubic systems [61, 62], but its application to the complex rare-earth based $\text{Nd}_2\text{Fe}_{14}\text{B}$ system remains to be further explored.

IV. CONCLUSIONS

In summary, we have carried out *ab-initio* informed atomistic spin model simulations to predict the temperature-dependent intrinsic properties of $\text{Nd}_2\text{Fe}_{14}\text{B}$ permanent magnets. The results are relevant for temperature-dependent micromagnetic simulations of Nd-Fe-B magnets. The main conclusions are summarized as:

(1) The Hamiltonian of the atomistic spin model for $\text{Nd}_2\text{Fe}_{14}\text{B}$ includes contributions from the Heisenberg exchange of Fe-Fe and Fe-Nd atomic pairs, the uniaxial single-ion anisotropy energy of Fe atoms, and the crystal-field energy of Nd ions. Specially, we approximately expand the crystal-field Hamiltonian of Nd ions into an energy formula featured by second, fourth, and sixth-order phenomenological anisotropy constants.

(2) Monte Carlo simulations of the atomistic spin model readily capture the Curie temperature T_c of $\text{Nd}_2\text{Fe}_{14}\text{B}$. After applying the temperature rescaling

strategy and the fitted rescaling parameter $\alpha = 1.802$, we show the calculated temperature dependence of saturation magnetization $M_s(T)$ agrees well with the experimental results, and the spin reorientation phenomenon at low temperature is well predicted.

(3) Constrained Monte Carlo simulations give the temperature-dependent total internal torque, from which we calculate the macroscopically effective second-, fourth-, and sixth-order anisotropy constants that match well with the experimental measurements. The calculated values at 300 K shows good consistency with literature reports, with K_1^{eff} , K_2^{eff} , and K_3^{eff} as 4.26, 0.15, and -0.10 MJ/m³, respectively.

(4) Mapping the atomistic magnetic moments to the continuum magnetization leads to the domain wall profile, which can be further fitted by hyperbolic functions to evaluate the domain wall width δ_w . Different domain wall configurations at low temperatures are identified. The calculated δ_w and its variance increases with temperature, and its value at 300 K is consistent with experimental observation. δ_w is found to scale with magnetization as a function of $m^{2.26}$.

(5) By using a general continuum formula with the exchange stiffness constant $A_e(T)$ as a parameter to describe the domain wall profile, we determine $A_e(T)$. A_e is found to decrease more slowly than K_1^{eff} with increasing temperature. The scaling behavior of the exchange stiffness with the normalized magnetization is found to be $A_e(T) \sim m$ at temperatures below 500 K and $A_e(T) \sim m^{1.55}$ at temperatures close to T_c .

ACKNOWLEDGMENT

Support from the German Science Foundation (DFG YI 165/1-1 and DFG XU 121/7-1) and the German federal state of Hessen through its excellence programme LOEWE RESPONSE is appreciated. M Yi acknowledges the support from the open project of State Key Lab for Strength and Vibration of Mechanical Structures (SV2017-KF-28) and the 15th Thousand Youth Talents Program of China. Dr Hongbin Zhang is acknowledged for his valuable comments. The authors also acknowledge the access to the Lichtenberg High Performance Computer of TU Darmstadt.

-
- [1] O. Gutfleisch, M. A. Willard, E. Brück, C. H. Chen, S. G. Sankar, and J. P. Liu, “Magnetic materials and devices for the 21st century: stronger, lighter, and more energy efficient,” *Advanced Materials* **23**, 821–842 (2011).
 - [2] KP Skokov and O Gutfleisch, “Heavy rare earth free, free rare earth and rare earth free magnets-vision and reality,” *Scripta Materialia* **154**, 289–294 (2018).
 - [3] K Hono and H Sepehri-Amin, “Prospect for HRE-free high coercivity Nd-Fe-B permanent magnets,” *Scripta Materialia* **151**, 6–13 (2018).
 - [4] XB Liu and Z Altounian, “The partitioning of Dy and Tb in NdFeB magnets: a first-principles study,” *Journal of Applied Physics* **111**, 07A701 (2012).
 - [5] Y Toga, T Suzuki, and A Sakuma, “Effects of trace elements on the crystal field parameters of Nd ions at the surface of $\text{Nd}_2\text{Fe}_{14}\text{B}$ grains,” *Journal of Applied Physics* **117**, 223905 (2015).
 - [6] T Suzuki, Y Toga, and A Sakuma, “Effects of deformation on the crystal field parameter of the Nd ions in $\text{Nd}_2\text{Fe}_{14}\text{B}$,” *Journal of Applied Physics* **115**, 17A703 (2014).

- (2014).
- [7] Y Tatetsu, S Tsuneyuki, and Y Gohda, “First-principles study of the role of Cu in improving the coercivity of Nd-Fe-B permanent magnets,” *Physical Review Applied* **6**, 064029 (2016).
 - [8] M Yi, H Zhang, O Gutfleisch, and B-X Xu, “Multiscale examination of strain effects in Nd-Fe-B permanent magnets,” *Physical Review Applied* **8**, 014011 (2017).
 - [9] H Tsuchiura, T Yoshioka, and P Novák, “First-principles calculations of crystal field parameters of Nd ions near surfaces and interfaces in Nd-Fe-B magnets,” *IEEE Transactions on Magnetics* **50**, 1–4 (2014).
 - [10] G Hrkac, TG Woodcock, C Freeman, A Goncharov, J Dean, T Schrefl, and O Gutfleisch, “The role of local anisotropy profiles at grain boundaries on the coercivity of Nd₂Fe₁₄B magnets,” *Applied Physics Letters* **97**, 232511 (2010).
 - [11] TG Woodcock, Y Zhang, G Hrkac, G Ciuta, NM Dempsey, T Schrefl, O Gutfleisch, and D Givord, “Understanding the microstructure and coercivity of high performance NdFeB-based magnets,” *Scripta Materialia* **67**, 536–541 (2012).
 - [12] H Sepehri-Amin, T Ohkubo, M Gruber, T Schrefl, and K Hono, “Micromagnetic simulations on the grain size dependence of coercivity in anisotropic Nd–Fe–B sintered magnets,” *Scripta Materialia* **89**, 29–32 (2014).
 - [13] J Fischbacher, A Kovacs, M Gusenbauer, H Oezelt, L Exl, S Bance, and T Schrefl, “Micromagnetics of rare-earth efficient permanent magnets,” *Journal of Physics D: Applied Physics* **51**, 193002 (2018).
 - [14] J Fidler and T Schrefl, “Micromagnetic modelling-the current state of the art,” *Journal of Physics D: Applied Physics* **33**, R135 (2000).
 - [15] M Yi, O Gutfleisch, and B-X Xu, “Micromagnetic simulations on the grain shape effect in Nd-Fe-B magnets,” *Journal of Applied Physics* **120**, 033903 (2016).
 - [16] P Toson, GA Zickler, and J Fidler, “Do micromagnetic simulations correctly predict hard magnetic hysteresis properties?” *Physica B: Condensed Matter* **486**, 142–150 (2016).
 - [17] T Helbig, K Loewe, S Sawatzki, M Yi, B-X Xu, and O Gutfleisch, “Experimental and computational analysis of magnetization reversal in (Nd, Dy)-Fe-B core shell sintered magnets,” *Acta Materialia* **127**, 498–504 (2017).
 - [18] GA Zickler, J Fidler, J Bernardi, T Schrefl, and A Asali, “A combined TEM/STEM and micromagnetic study of the anisotropic nature of grain boundaries and coercivity in Nd-Fe-B magnets,” *Advances in Materials Science and Engineering* **2017**, 6412042 (2017).
 - [19] S Erokhin and D Berkov, “Optimization of nanocomposite materials for permanent magnets: Micromagnetic simulations of the effects of intergrain exchange and the shapes of hard grains,” *Physical Review Applied* **7**, 014011 (2017).
 - [20] S Bance, J Fischbacher, and T Schrefl, “Thermally activated coercivity in core-shell permanent magnets,” *Journal of Applied Physics* **117**, 17A733 (2015).
 - [21] S Bance, J Fischbacher, A Kovacs, H Oezelt, F Reichel, and T Schrefl, “Thermal activation in permanent magnets,” *JOM* **67**, 1350–1356 (2015).
 - [22] S Hirosawa, M Nishino, and S Miyashita, “Perspectives for high-performance permanent magnets: applications, coercivity, and new materials,” *Advances in Natural Sciences: Nanoscience and Nanotechnology* **8**, 013002 (2017).
 - [23] RFL Evans, D Givord, R Cuadrado, T Shoji, M Yano, M Ito, A Manabe, G Hrkac, T Schrefl, and RW Chantrell, “Atomistic spin dynamics and temperature dependent properties of Nd₂Fe₁₄B,” 8th Joint European Magnetic Symposia, 21-26 August, 2016.
 - [24] Y Toga, M Matsumoto, S Miyashita, H Akai, S Doi, T Miyake, and A Sakuma, “Monte Carlo analysis for finite-temperature magnetism of Nd₂Fe₁₄B permanent magnet,” *Physical Review B* **94**, 174433 (2016).
 - [25] M Nishino, Y Toga, S Miyashita, H Akai, A Sakuma, and S Hirosawa, “Atomistic-model study of temperature-dependent domain walls in the neodymium permanent magnet Nd₂Fe₁₄B,” *Physical Review B* **95**, 094429 (2017).
 - [26] H Tsuchiura, T Yoshioka, and P Novák, “Bridging atomistic magnetism and coercivity in Nd-Fe-B magnets,” *Scripta Materialia* **154**, 248–252 (2018).
 - [27] S Miyashita, M Nishino, Y Toga, T Hinokihara, T Miyake, S Hirosawa, and A Sakuma, “Perspectives of stochastic micromagnetism of Nd₂Fe₁₄B and computation of thermally activated reversal process,” *Scripta Materialia* **154**, 259–265 (2018).
 - [28] SC Westmoreland, RFL Evans, G Hrkac, T Schrefl, GT Zimanyi, M Winklhofer, N Sakuma, M Yano, A Kato, T Shoji, A Manabe, M Ito, and RW Chantrell, “Multiscale model approaches to the design of advanced permanent magnets,” *Scripta Materialia* **148**, 56–62 (2018).
 - [29] B Skubic, J Hellsvik, L Nordström, and O Eriksson, “A method for atomistic spin dynamics simulations: implementation and examples,” *Journal of Physics: Condensed Matter* **20**, 315203 (2008).
 - [30] RFL Evans, WJ Fan, P Churemart, TA Ostler, MOA Ellis, and RW Chantrell, “Atomistic spin model simulations of magnetic nanomaterials,” *Journal of Physics: Condensed Matter* **26**, 103202 (2014).
 - [31] O Eriksson, A Bergman, L Bergqvist, and J Hellsvik, “Atomistic spin dynamics: Foundations and applications,” Oxford University Press (2017).
 - [32] Y Toga, M Nishino, S Miyashita, T Miyake, and A Sakuma, “Anisotropy of exchange stiffness based on atomic-scale magnetic properties in the rare-earth permanent magnet Nd₂Fe₁₄B,” *Physical Review B* **98**, 054418 (2018).
 - [33] M Yamada, H Kato, H Yamamoto, and Y Nakagawa, “Crystal-field analysis of the magnetization process in a series of Nd₂Fe₁₄B-type compounds,” *Physical Review B* **38**, 620 (1988).
 - [34] RJ Elliott and KWH Stevens, “The theory of magnetic resonance experiments on salts of the rare earths,” *Proc. R. Soc. Lond. A* **218**, 553–566 (1953).
 - [35] AJ Freeman and RE Watson, “Theoretical investigation of some magnetic and spectroscopic properties of rare-earth ions,” *Physical Review* **127**, 2058 (1962).
 - [36] Y Miura, H Tsuchiura, and T Yoshioka, “Magnetocrystalline anisotropy of the Fe-sublattice in Y₂Fe₁₄B systems,” *Journal of Applied Physics* **115**, 17A765 (2014).
 - [37] AI Liechtenstein, MI Katsnelson, VP Antropov, and VA Gubanov, “Local spin density functional approach to the theory of exchange interactions in ferromagnetic metals and alloys,” *Journal of Magnetism and Magnetic Materials* **67**, 65–74 (1987).
 - [38] MJ Han, T Ozaki, and J Yu, “Electronic structure, magnetic interactions, and the role of ligands in Mn_n

- ($n=4,12$) single-molecule magnets,” *Physical Review B* **70**, 184421 (2004).
- [39] H Yoon, TJ Kim, J-H Sim, S W Jang, T Ozaki, and MJ Han, “Reliability and applicability of magnetic-force linear response theory: Numerical parameters, predictability, and orbital resolution,” *Physical Review B* **97**, 125132 (2018).
- [40] TJ Kim, H Yoon, and MJ Han, “Calculating magnetic interactions in organic electrides,” *Physical Review B* **97**, 214431 (2018).
- [41] SW Jang, S Ryee, H Yoon, and MJ Han, “Charge density functional plus u theory of LaMnO_3 : Phase diagram, electronic structure, and magnetic interaction,” *Physical Review B* **98**, 125126 (2018).
- [42] K-D Durst and H Kronmüller, “Determination of intrinsic magnetic material parameters of $\text{Nd}_2\text{Fe}_{14}\text{B}$ from magnetic measurements of sintered $\text{Nd}_{15}\text{Fe}_{77}\text{B}_8$ magnets,” *Journal of Magnetism and Magnetic Materials* **59**, 86–94 (1986).
- [43] S Hirosawa, Y Matsuura, H Yamamoto, S Fujimura, M Sagawa, and H Yamauchi, “Magnetization and magnetic anisotropy of $\text{R}_2\text{Fe}_{14}\text{B}$ measured on single crystals,” *Journal of Applied Physics* **59**, 873–879 (1986).
- [44] D Givord, HS Li, and RP de la B  thie, “Magnetic properties of $\text{Y}_2\text{Fe}_{14}\text{B}$ and $\text{Nd}_2\text{Fe}_{14}\text{B}$ single crystals,” *Solid State Communications* **88**, 907–910 (1993).
- [45] P Asselin, RFL Evans, J Barker, RW Chantrell, R Yanes, O Chubykalo-Fesenko, D Hinzke, and U Nowak, “Constrained Monte Carlo method and calculation of the temperature dependence of magnetic anisotropy,” *Physical Review B* **82**, 054415 (2010).
- [46] AV Ruban, S Shallcross, SI Simak, and HL Skriver, “Atomic and magnetic configurational energetics by the generalized perturbation method,” *Physical Review B* **70**, 125115 (2004).
- [47] J Staunton, BL Gyorffy, GM Stocks, and J Wadsworth, “The static, paramagnetic, spin susceptibility of metals at finite temperatures,” *Journal of Physics F: Metal Physics* **16**, 1761 (1986).
- [48] RFL Evans, U Atxitia, and RW Chantrell, “Quantitative simulation of temperature-dependent magnetization dynamics and equilibrium properties of elemental ferromagnets,” *Physical Review B* **91**, 144425 (2015).
- [49] O Yamada, H Tokuhara, F Ono, M Sagawa, and Y Matsuura, “Magnetocrystalline anisotropy in $\text{Nd}_2\text{Fe}_{14}\text{B}$ intermetallic compound,” *Journal of Magnetism and Magnetic Materials* **54**, 585–586 (1986).
- [50] R Sasaki, D Miura, and A Sakuma, “Theoretical evaluation of the temperature dependence of magnetic anisotropy constants of $\text{Nd}_2\text{Fe}_{14}\text{B}$: Effects of exchange field and crystal field strength,” *Applied Physics Express* **8**, 043004 (2015).
- [51] YG Pastushenkov, A Forkl, and H Kronm  ller, “Temperature dependence of the domain structure in $\text{Fe}_{14}\text{Nd}_2\text{B}$ single crystals during the spin-reorientation transition,” *Journal of Magnetism and Magnetic Materials* **174**, 278–288 (1997).
- [52] YG Pastushenkov, NP Suponev, T Dragon, and H Kronm  ller, “The magnetic domain structure of $\text{Fe}_{14}\text{Nd}_2\text{B}$ single crystals between 135 and 4 K and the low-temperature magnetization reversal process in Fe-Nd-B permanent magnets,” *Journal of Magnetism and Magnetic Materials* **196**, 856–858 (1999).
- [53] Y Sun and C Beckermann, “Sharp interface tracking using the phase-field equation,” *Journal of Computational Physics* **220**, 626–653 (2007).
- [54] A Hubert and R Sch  fer, “Magnetic domains: the analysis of magnetic microstructures,” Springer Science & Business Media, 2018.
- [55] H Kronm  ller and M F  hnle, “Micromagnetism and the microstructure of ferromagnetic solids,” Cambridge University Press, 2003.
- [56] K Ono, N Inami, K Saito, Y Takeichi, M Yano, T Shoji, A Manabe, A Kato, Y Kaneko, D Kawana, et al., “Observation of spin-wave dispersion in Nd-Fe-B magnets using neutron Brillouin scattering,” *Journal of Applied Physics* **115**, 17A714 (2014).
- [57] Y Zhu and MR McCartney, “Magnetic-domain structure of $\text{Nd}_2\text{Fe}_{14}\text{B}$ permanent magnets,” *Journal of Applied Physics* **84**, 3267–3272 (1998).
- [58] SJ Lloyd, JC Loudon, and PA Midgley, “Measurement of magnetic domain wall width using energy-filtered fresnel images,” *Journal of Microscopy* **207**, 118–128 (2002).
- [59] M Beleggia, MA Schofield, Y Zhu, and G Pozzi, “Quantitative domain wall width measurement with coherent electrons,” *Journal of Magnetism and Magnetic Materials* **310**, 2696–2698 (2007).
- [60] R Moreno, RFL Evans, S Khmelevskyi, MC Mu  noz, RW Chantrell, and O Chubykalo-Fesenko, “Temperature-dependent exchange stiffness and domain wall width in Co,” *Physical Review B* **94**, 104433 (2016).
- [61] U Atxitia, D Hinzke, O Chubykalo-Fesenko, U Nowak, H Kachkachi, ON Mryasov, RF Evans, and RW Chantrell, “Multiscale modeling of magnetic materials: Temperature dependence of the exchange stiffness,” *Physical Review B* **82**, 134440 (2010).
- [62] LS Campana, A Caramico D’Auria, M D’Ambrosio, U Esposito, L De Cesare, and G Kamieniarz, “Spectral-density method for classical systems: Heisenberg ferromagnet,” *Physical Review B* **30**, 2769 (1984).